

Article

Acid Modification of the Unsupported NiMo Catalysts by Y-Zeolite Nanoclusters

Chengwu Dong, Changlong Yin *, Tongtong Wu, Zhuyan Wu, Dong Liu and Chenguang Liu

State Key Laboratory of Heavy Oil Processing, Key Laboratory of Catalysis,
China National Petroleum Corporation (CNPC), China University of Petroleum, Qingdao 266580, China

* Correspondence: yincl@upc.edu.cn; Tel.: +86-532-86984629

Received: 7 May 2019; Accepted: 2 July 2019; Published: 4 July 2019



Abstract: Unsupported NiMo catalyst has high hydrogenation activity due to its high active site distribution. However, low specific surface area and pore distribution greatly limit the efficient utilization of the active components. The Y-zeolite nanoclusters were hydrothermally synthesized and introduced into the unsupported NiMo catalysts from a layered nickel molybdate complex oxide. The XRD, N₂ adsorption-desorption, FT-IR, Py-IR, SEM, NH₃-TPD, and TEM were used to characterize all catalysts. The dibenzothiophene (DBT) hydrodesulfurization (HDS) reaction was performed in a continuous high pressure microreactor. The results showed that the specific surface area, pore volume, and average pore size of the unsupported NiMo catalysts were greatly increased by the Y-zeolite nanoclusters, and a more dispersed structure was produced. Furthermore, the Lewis acid and total acid content of the unsupported NiMo catalysts were greatly improved by the Y-zeolite nanoclusters. The HDS results showed that the unsupported NiMo catalysts modified by the nanoclusters had the same high desulfurization efficiency as the unmodified catalyst, but had more proportion of direct desulfurization (DDS) products. The results offer an alternative to reducing hydrogen consumption and save cost in the production of ultra clean diesel.

Keywords: unsupported NiMo catalysts; Y-zeolite nanoclusters; modification; hydrodesulfurization; ultra clean diesel

1. Introduction

Unsupported hydrogenation catalysts, such as NiMo, CoMo, NiW, NiMoW, CoMoW, etc., have high activity which is 3-4 times greater in hydrodesulfurization (HDS) activity than commonly used industrial catalysts [1–5]. Compared with the supported hydrogenation catalysts (NiMo/Al₂O₃, CoMo/Al₂O₃, and NiMoW/Al₂O₃, etc.) [6–8], the unsupported hydrogenation catalysts are made up of entirely active components and auxiliaries, and not limited by the lack of active components. The unsupported catalysts are usually synthesized by a co-precipitation method [9,10], and the catalyst precursors are mainly ammonium nickel molybdate crystals [11,12], which produce a lower specific surface area and have less pore distribution than the supported catalysts. Additionally, the unsupported catalysts have high HDS activity only after activation. The main activation methods are presulfidation, which mainly includes a gas phase (H₂S/H₂) [12–14] and liquid phase (CS₂/H₂) [15,16]. The sulfidation reagent is difficult to enter the inner of the unsupported catalysts due to its lower pore distribution, and only the active components distributed on the outer surface are sulfided, which greatly reduces the utilization rate of the active component and causes great waste. To increase the specific surface area and pore distribution of the unsupported hydrogenation catalysts, a pore-expanding agent, such as methylcellulose, was added before forming by Yin et al. [17], which produces more pore structures for the unsupported hydrogenation catalysts after calcination. In addition, hydrothermal aging was also used to treat the unsupported catalyst precursors to improve the dispersion of the active

components [17], and the results showed that the specific surface area, pore volume, and average pore diameter of the unsupported catalysts were obviously improved after aging. At the same time, the hydrotreating activity was greatly improved. However, the higher hydrogenation activity of the unsupported catalysts can produce deep hydrogenation for the impurities in diesel, which increases the hydrogen consumption and the complexity of the reaction [18]. It is not conducive to efficient and low-cost industrial production.

Furthermore, unsupported catalysts have weak acidity due to the lack of the support [18]. Solid acids including Lewis and Brønsted acid sites are related to the isomerization and cracking activity of the catalyst [19–21], and play an important role in the catalytic reaction. The suitable Lewis and Brønsted acid sites are beneficial to the improvement of the isomerization and cracking activity of the catalyst [22,23]. However, the unsupported catalysts have only the weak Lewis acid site [18], and it can only be used for hydrogenation but not for isomerization and cracking reactions, which leads to great limitations. To improve the acidity of the unsupported catalysts, the alumina was added to the unsupported catalysts, but the acidity of the unsupported catalysts was not significantly improved due to the weak acidity of alumina. Zeolites with strong acidity were also introduced into the unsupported catalysts, but the final catalysts produced the lower strength, and it was not conducive to industrial application. The zeolite nanoclusters are the secondary structural units of zeolite, and their properties have been studied before [24–28]. Recently, the ZSM-5 zeolite nanoclusters were used to modify the zeolite FDU-12 [29], the results showed that the introduction of the ZSM-5 zeolite nanoclusters resulted in the production of satisfactory pore properties, appropriate acidic properties, and preferable dispersed active components, which could be beneficial to the improvement of hydrodesulfurization activity. Moreover, more gases can be produced due to the thermal decomposition of the template, so more pore structures can be produced for the unsupported catalysts after calcination.

In this work, Y-zeolite nanoclusters were synthesized by hydrothermal method, and the Y-zeolite nanoclusters with different crystallization time were successfully introduced into the unsupported catalysts to improve the dispersion and the acidity of the unsupported catalysts. The properties of the unsupported catalysts before and after modification were characterized by XRD, N₂ adsorption-desorption, FT-IR, Py-IR, SEM, NH₃-TPD, and TEM. The dibenzothiophene (DBT) HDS activity of all catalysts was evaluated in a continuous high pressure microreactor, where the unmodified unsupported catalyst (NiMo-1.5) was taken as a reference. The effects of the Y-zeolite nanoclusters on the physico-chemical properties of unsupported catalyst were discussed systematically.

2. Experimental

2.1. Synthesis of Unsupported NiMo Catalysts

The unsupported NiMo catalysts were prepared according to the previously reported method [10,18,30]. The unsupported NiMo catalyst precursor was synthesized by preparing an aqueous solution of ammonium heptamolybdate, ammonia water, and nickel nitrate with a molar ratio of Ni and Mo (1.5:1). Typically, 200 mL deionized water in a flask was heated to 60 °C firstly. Then the proper amount of nickel nitrate hexahydrate (Ni(NO₃)₂·6H₂O) and ammonium heptamolybdate solution were slowly added into the flask and stirred. When the temperature was stabilized to 93 °C, the ammonium hydroxide (28.8% NH₃) was added under stirring until the mixture changed from a suspension to a clear solution and stopped dropping, finally the pH was about 12 for the clear solution, and the clear aqueous solution was heated at 93 °C for 10 h under stirring to obtain the turbid liquid. The turbid liquid was aged overnight under stirring, and filtered, washed with deionized water, and dried 12 h at 100 °C. Then the unsupported NiMo catalyst precursor was synthesized. The precursor was calcined at 350 °C for 4 h. The unsupported NiMo catalyst (NiMo-1.5) was obtained.

2.2. Synthesis of Y-Zeolite Nanoclusters

Y-zeolite nanoclusters were synthesized hydrothermally by preparing a clear aqueous solution with a molar ratio of $1.0\text{SiO}_2:0.15\text{Al}_2\text{O}_3:0.6\text{TMA}_2\text{O}:40\text{H}_2\text{O}$ [31]. Typically, a proper amount of tetramethylammonium hydroxide (TMAOH, 25 wt%) and aluminum isopropoxide ($\text{Al}(\text{OiPr})_3$, 98 wt%) were mixed together and stirred at room temperature for 3 h. Then the mixture of tetraethoxysilane (TEOS, 98 wt%) and deionized water was added under stirring. The final clear solution was hydrothermally crystallized at 120 °C for 10, 24, 36, 60, and 72 h at a Teflon-lined stainless steel autoclave. The liquid Y-zeolite nanoclusters with different crystallization times were obtained.

2.3. Synthesis of Unsupported NiMo Catalysts Modified by Y-Zeolite Nanoclusters

Twenty grams of liquid Y-zeolite nanoclusters with different crystallization times were dripped into the unsupported NiMo catalyst precursor turbid liquid after the aqueous solution of nickel nitrate hexahydrate, ammonium heptamolybdate, and ammonia water was reacted for 9 h. After an hour, the heating was stopped, and the mixture was aged overnight under stirring to obtain the complexes of unsupported NiMo catalyst precursors and Y-zeolite nanoclusters. The complexes were filtered, washed with deionized water, and dried 12 h at 100 °C to get the modified unsupported NiMo catalyst precursor. And the precursor was calcined at 350 °C for 4 h to obtain the modified unsupported NiMo catalysts. The catalysts after modification were labeled as Y-NiMo-10h, Y-NiMo-24h, Y-NiMo-36h, Y-NiMo-60h, and Y-NiMo-72h, respectively.

2.4. Characterization of Catalysts

X-ray diffraction (XRD) analysis was performed with an X'Pert Pro MPD instrument (Panalytical, Almelo, Netherlands) using a $\text{Cu K}\alpha$ operated at 45 kV and 40 mA. The samples were ground to powder and pressed into a smooth sheet before measurement. The specific surface area and pore structure of the unsupported NiMo catalyst were determined by N_2 adsorption-desorption using a Tristar3000 multifunctional adsorption instrument (Micromeritics, Norcross, GA, USA) with the N_2 adsorption temperature of -196 °C, and the pore structure properties (specific surface area, pore volume, and average pore size) were calculated by BET and BJH methods. The FT-IR analysis was carried out via a Nexus infrared spectrometer (Nicolet, Madison, WI, USA) with the background of KBr. The Py-IR analysis was performed by Bruker Vertex-70. Before measurement, the samples were calcined at 300 °C for 3 h, and pyridine was adsorbed for 24 h at room temperature and vacuum desorbed at 150 °C for 5 h. The NH_3 temperature-programmed desorption (NH_3 -TPD) and H_2 temperature-programmed reduction (H_2 -TPR) of all catalysts were performed on a Micromeritics AutoChem HP 2950 Chemisorption Analyzer (Micromeritics, Norcross, GA, USA) with a thermal conductivity detector (TCD). The morphology of the all samples was investigated by a cold field emission scanning electron microscope (SEM) (S-4800, Hitachi Company, Tokyo, Japan). TEM measurements were performed on a high resolution electron transmission microscope (JEM-2100, Hitachi Company, Tokyo, Japan) operated at 200 KV. The slab length and stacking layers of MoS_2 were statistically analyzed by about 15 micrographs, including 200 particles for each catalyst. The average slab length and stacking layers of MoS_2 were calculated according to Equations (1) and (2) [32,33], and The dispersion of Mo atoms on the edge surface of the MoS_2 crystals (f_{Mo}) was calculated by Equation (3) [34,35]:

$$L_A = \frac{\sum_{i=1}^E n_i L_i}{\sum_{i=1}^t n_i} \quad (1)$$

$$N_A = \frac{\sum_{i=1}^t n_i N_i}{\sum_{i=1}^t n_i} \quad (2)$$

$$f_{Mo} = \frac{\sum_{i=1}^n (6x_i - 6)}{\sum_{i=1}^n (3x_i^2 - 3x_i + 1)} \quad (3)$$

where L_i is the slab length, and n_i of Equation (1) is the number of MoS₂ slabs whose slab length is L_i . For Equation (2), N_i represents the stacking layers, n_i represents the number of MoS₂ particles whose stacking layer number is N_i . For Equation (3), x_i is the number of atoms along one edge of a MoS₂ slab determined from $L = 3.2(2x_i - 1)A$, and n represents the total number of MoS₂ slabs shown in the TEM micrographs.

2.5. Catalytic Activity Evaluation

The HDS performance of the unsupported NiMo catalysts before and after modification was evaluated using a 1.0 wt% DBT/n-heptane solution. The HDS reaction for DBT was conducted in a fixed bed high pressure microreactor loaded with 1 mL catalysts (20–40 mesh) diluted with 2 mL quartz (20–40 mesh). The catalysts were presulfided in a mixture of 3.0 wt% CS₂/n-heptane solution at 330 °C for 8 h (3.0 MPa, H₂-to-oil ratio of 300, liquid hourly space velocity (LHSV) of 6.0 h⁻¹). Reaction tests were performed after sulfidation, and the reaction conditions were 300 °C, 3.0 MPa, H₂-to-oil ratio of 300, liquid hourly space velocity (LHSV) of 10 h⁻¹. The liquid samples were collected and analyzed by a Varian 3800 gas chromatography. Additionally, the desulfurization pathways, including direct desulfurization (DDS) and hydrogenation (HYD), were defined by Equations (4) and (5), and the selectivity of the desulfurization pathway can be reflected by DDS/HYD:

$$DDS = \frac{BP \times 100\%}{THDBT + HHDBT + BP + CHB + BCH} \quad (4)$$

$$HYD = \frac{(THDBT + HHDBT + CHB + BCH) \times 100\%}{THDBT + HHDBT + BP + CHB + BCH} \quad (5)$$

3. Results and Discussion

3.1. Characterization of Y-Zeolite Nanoclusters

Figure 1 shows the XRD spectra of Y-zeolite nanoclusters with different crystallization time. As shown in Figure 1, when the crystallization time is less than 72 h, all samples are in an amorphous state. When the crystallization time is prolonged to 144 h, the characteristic diffraction peaks of the Y-zeolite were detected at $2\theta = 6.2^\circ, 10.3^\circ, 21.8^\circ, 26.5^\circ,$ and 31.3° , respectively [31,36], which indicates that the Y-zeolite can be successfully synthesized. Therefore, no Y-zeolite crystals were formed in the samples with crystallization time less than 72 h, and these samples could be considered as the Y-zeolite nanoclusters.

The skeletal structure of Y-zeolites at different crystallization times were detected by FT-IR spectra, and the results were shown in Figure 2.

All samples show the absorption peaks at 440–470 cm⁻¹, which can be attributed to the characteristic absorption peak of Si–O bond in the tetrahedral TO₄ structure (T = Si, Al) materials [37,38]. Additionally, when the crystallization time is 10 and 24 h, the characteristic absorption band at about 570 cm⁻¹ was detected, which is attributed to the characteristic absorption peak of the Y-zeolite five-membered ring structure [38,39]. However, this peak shifts to the higher wavenumber from 570 to 590 cm⁻¹ with the prolongation of the crystallization time, which is the result of the aggregation of the five-membered ring structure. In addition, when the crystallization time is 0 h, the obvious absorption peak at 614 cm⁻¹ is the characteristic absorption peak of the Si–O–Si structure of silicate [24,26,40], and the peak shifts to the higher wavenumber from 614 to 700 cm⁻¹ with the prolongation of the crystallization time, the reason is that the silicates are converted with the prolongation of the crystallization time. Furthermore, the obvious absorption bands between 1300

and 1700 cm^{-1} were detected, which could be attributed to the tetramethylammonium hydroxide (TMAOH), indicating that the template was encapsulated in the Y-zeolite nanoclusters.

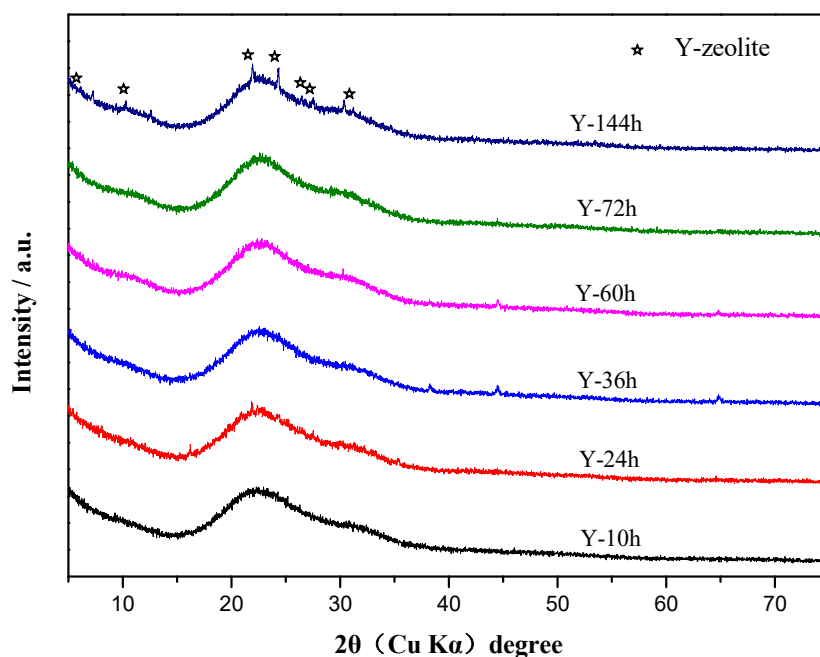


Figure 1. XRD patterns of Y-zeolite nanoclusters with different crystallization times.

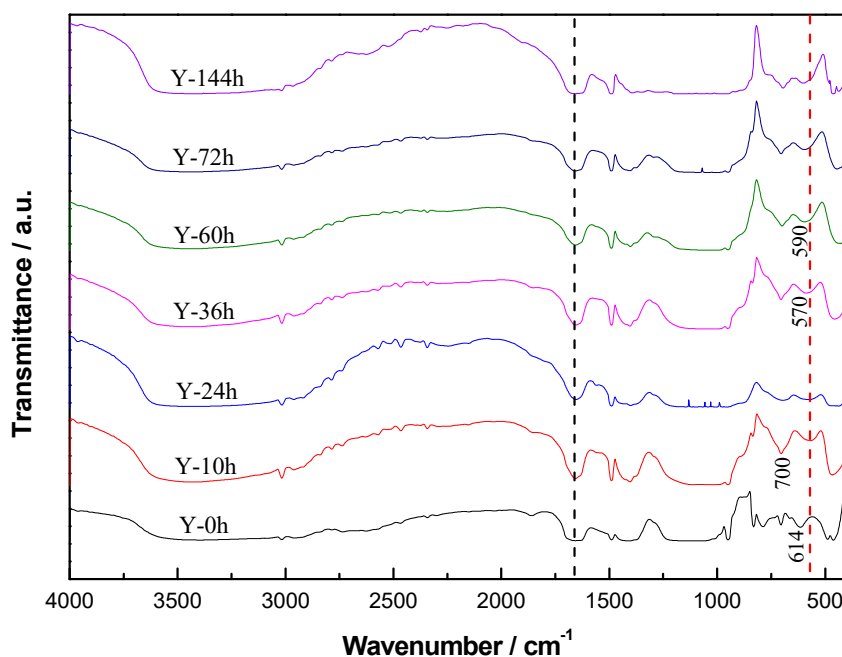


Figure 2. FT-IR spectra of Y-zeolite nanoclusters after different crystallization times.

3.2. Characterization of the Modified Unsupported NiMo Catalysts

The pore structure distribution of the unsupported NiMo catalyst modified by the Y-zeolite nanocluster is shown in Table 1. Table 1 shows that the specific surface area and pore volume of the unsupported NiMo catalyst modified by the Y-zeolite nanocluster are greatly improved, the reason is that the TMAOH encapsulated in the Y-zeolite nanocluster structural unit can be thermally decomposed into volatile gases, and the volatilization of these gases can play a role in pore formation. In addition, as shown in Figure 3, the introduction of Y-zeolite nanoclusters improved the pore size, and broadened

the pore size range of unsupported Ni-Mo catalysts. However, the average pore size of the Y-NiMo-72h is only 3.65 nm less than that of the NiMo-1.5 (3.99 nm), the main reason is that the Y-zeolite nanocluster can gradually grow into larger particles with the prolongation of the crystallization time. A larger Y-zeolite nanocluster particle could destroy the macropores of the catalyst to produce more relatively small pores, so that the overall pore diameter is reduced. Additionally, the specific surface area of the Y-zeolite nanoclusters is $577 \text{ m}^2 \cdot \text{g}^{-1}$ which is much larger than the modified catalyst. The reason is that the structure of the nanoclusters will be changed greatly than that of the pure nanoclusters after the zeolite nanoclusters are introduced to unsupported NiMo catalysts. On the other hand, when the structure of the Y-zeolite nanoclusters was measured by the N_2 adsorption instrument, high-temperature treatment was required. In this process, the properties of the zeolite nanoclusters could be changed greatly, therefore, there is a great difference in the specific surface area between the Y-zeolite nanoclusters and the modified catalysts.

Table 1. Pore structure of the modified unsupported NiMo catalysts.

Samples	$S_{\text{BET}}^a / \text{m}^2 \cdot \text{g}^{-1}$	$V_p^b / \text{cm}^3 \cdot \text{g}^{-1}$	D_p^c / nm
NiMo-1.5	67	0.09	3.99
Y-zeolite nanoclusters	577	0.13	2.75
Y-NiMo-10h	131	0.20	4.66
Y-NiMo-24h	126	0.17	4.10
Y-NiMo-36h	137	0.20	4.45
Y-NiMo-60h	158	0.21	4.04
Y-NiMo-72h	176	0.20	3.65

^a S_{BET} : BET surface area. ^b V_p : Pore volume, calculated by the BJH method. ^c D_p : Average pore diameter, calculated by the BJH method from the desorption branch of the isotherms.

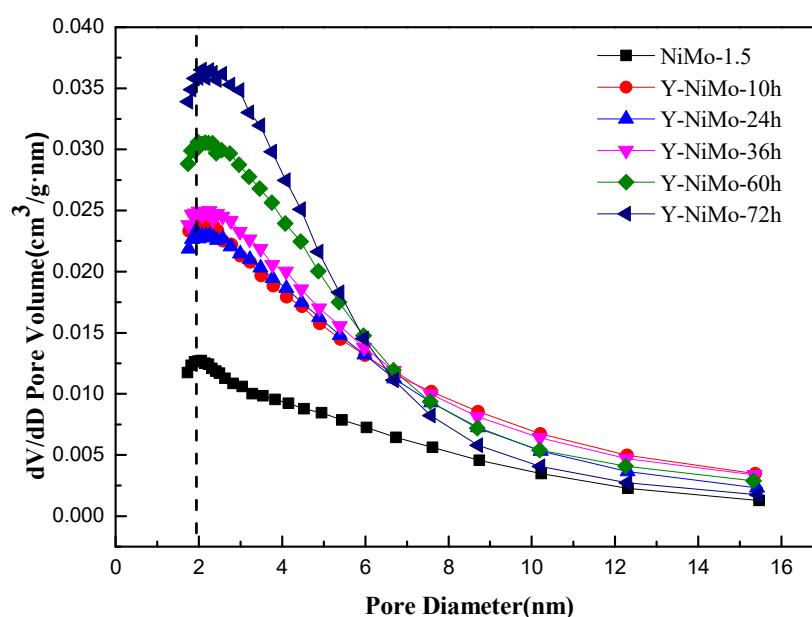


Figure 3. The pore size distribution of different unsupported Ni-Mo catalysts.

The SEM diagrams of the unsupported NiMo catalyst before and after modification were shown in Figure 4. The octahedral structures can be found in catalyst NiMo-1.5, which can be attributed to ammonium nickel molybdate crystal phase [18,41,42]. After modification, the octahedral ammonium nickel molybdate crystal phases disappear, the whole structure is in an amorphous state, indicating that the crystallization of ammonium nickel molybdate can be restricted by the Y-zeolite nanoclusters, and the same results are shown by the XRD (Figure 5). Additionally, the introduction of the Y-zeolite

nanoclusters produces a more dispersed structure for the unsupported NiMo catalysts, which can improve the dispersion and utilization of active components.

Figure 6A,B show the FT-IR spectra of different unsupported NiMo catalysts before and after calcination. Before calcination, the catalyst NiMo-1.5 shows five obvious absorption bands at about 486, 870, 1282, 1385, and 1629 cm^{-1} . The absorption peaks at 486 and 1282 cm^{-1} can be attributed to the Ni–O bond structures. The FT-IR peak at 1000–700 cm^{-1} is the Mo–O–Mo groups [10,30]. The absorption peaks at 1385 and 1629 cm^{-1} belong to the amino group of the ammonium-containing substance [10]. For modified unsupported NiMo catalysts, a new absorption peak was detected at about 1051 cm^{-1} , which is the characteristic absorption peak of the Si–O–Si structure [43–45], indicating that the Y-zeolite nanoclusters were successfully introduced into the unsupported NiMo catalysts. After calcination, the catalyst NiMo-1.5 retains the adsorption bands at 1282, 1385, and 1629 cm^{-1} , but the adsorption band at about 1385 cm^{-1} almost completely disappears, indicating that the unsupported NiMo catalysts modified by Y-zeolite nanoclusters are easier to be converted into an oxidized structure. In addition, the adsorption band strength at 1629 cm^{-1} decreases after calcination, which is the result of the thermal decomposition of the templates.

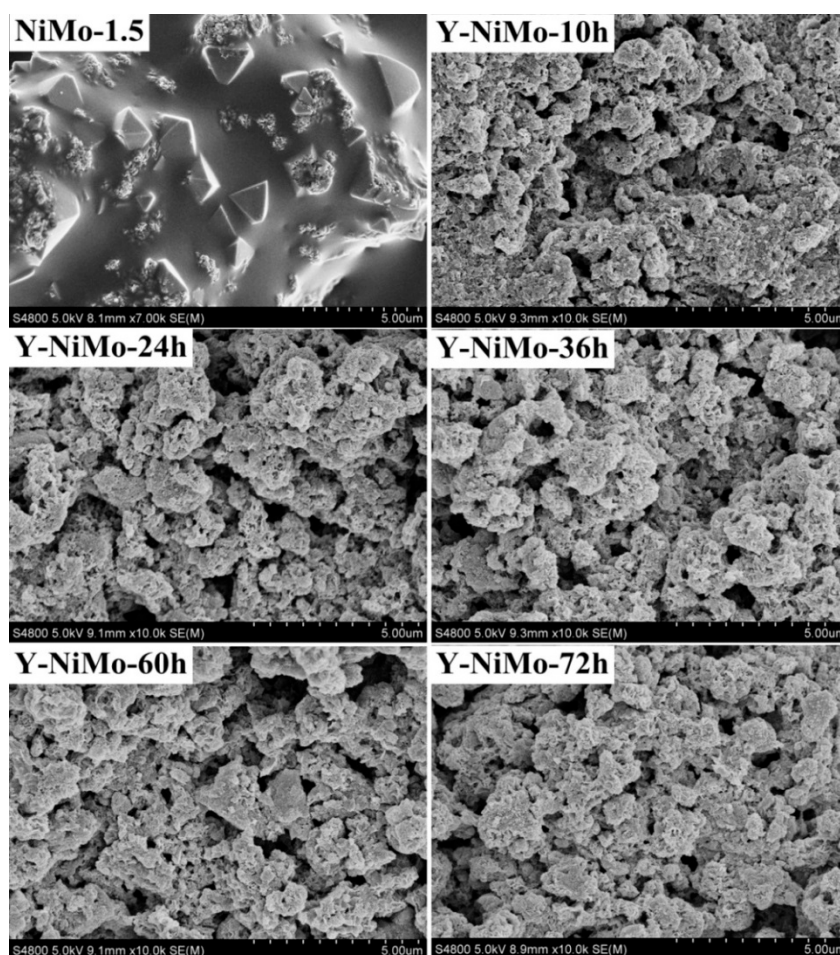


Figure 4. SEM of different unsupported NiMo catalysts.

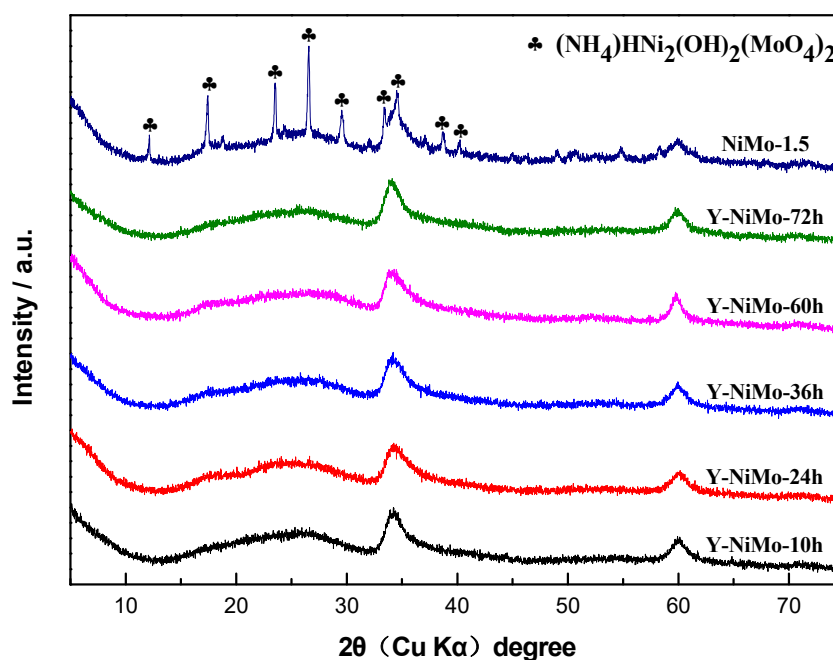


Figure 5. XRD patterns of different unsupported Ni-Mo catalysts.

Figure 7 and Table 2 show the Py-IR spectra and acid amount distributions of unsupported NiMo catalysts modified by Y-zeolite nanoclusters. As shown in Figure 7 and Table 2, the Y-zeolite nanoclusters Y-36h and Y-72h have all Lewis and Brønsted acid [46], but the unsupported NiMo catalysts modified by Y-zeolite nanoclusters have only Lewis acid, Brønsted acid was not detected, and the Lewis acid is obviously stronger than the unmodified catalyst. It may be that the Brønsted acid site could not be detected due to the weak Brønsted acid and low addition of the Y-zeolite nanoclusters. On the other hand, the Ni^{2+} remaining in the unsupported NiMo catalyst could replace the H^+ of the Si–OH–Al to produce more Lewis acid sites.

Table 2. Amounts and distributions of Lewis and Brønsted acid sites of different catalysts (mmol/g).

Samples	L (1447 cm^{-1})	B (1540 cm^{-1})	L + B(1490 cm^{-1})
Y-36h	0.357	0.113	0.295
Y-72h	0.157	0.227	0.260
NiMo-1.5	0.137	0	0.083
Y-NiMo-10h	0.390	0	0.132
Y-NiMo-24h	0.302	0	0.101
Y-NiMo-36h	0.305	0	0.105
Y-NiMo-60h	0.382	0	0.104
Y-NiMo-72h	0.342	0	0.117

Figure 8 and Table 3 show the NH_3 -TPD diagram and relative acid content of the unsupported NiMo catalysts modified by the Y-zeolite nanoclusters. All catalysts show the stronger peak at 100–300 °C and a weaker peak at 400–550 °C. The peak between 100 and 300 °C is a weak acid peak, and the peak between 400 and 550 °C can be classified as a strong acid peak, indicating that the unsupported NiMo catalysts before and after modification are mainly weak acid. Additionally, the peak area of the unsupported NiMo catalysts modified by Y-zeolite nanoclusters is obviously larger than that of the unmodified catalyst, and Table 3 also show higher relative acid content for modified unsupported NiMo catalysts, which indicates that the total acid content of the unsupported NiMo catalyst is obviously improved after the introduction of the Y-zeolite nanoclusters. Additionally, compared with the unmodified unsupported NiMo catalyst, the modified catalysts also show a weak desorption

peak at 550–750 °C, which should be the deoxidization peak produced by thermal decomposition of template (TMAOH) in Y-zeolite nanoclusters and unsupported NiMo catalysts.

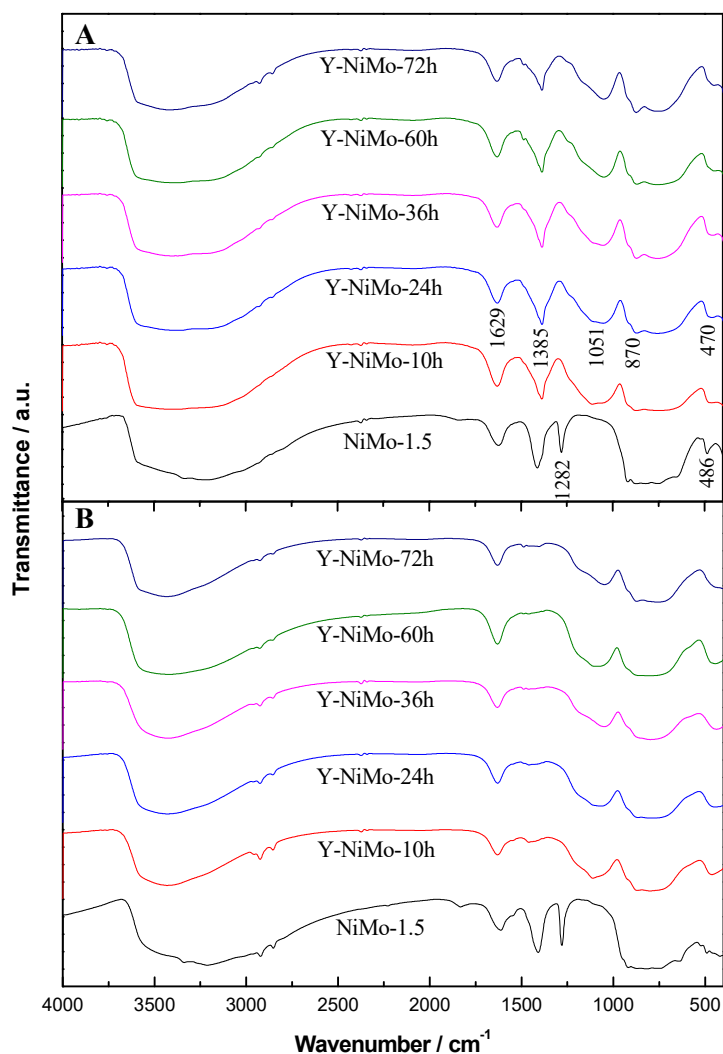


Figure 6. FT-IR of different unsupported NiMo catalysts (before calcination (A); and after calcination (B)).

Table 3. The relative acid content of the unsupported NiMo catalysts before and after modification.

Samples	100–300 °C	300–400 °C	400–550 °C
NiMo-1.5	61.034	23.269	15.697
Y-NiMo-10h	144.208	46.715	43.576
Y-NiMo-24h	134.164	41.182	31.856
Y-NiMo-36h	156.233	46.907	37.488
Y-NiMo-60h	160.110	47.368	42.105
Y-NiMo-72h	149.215	47.091	45.245

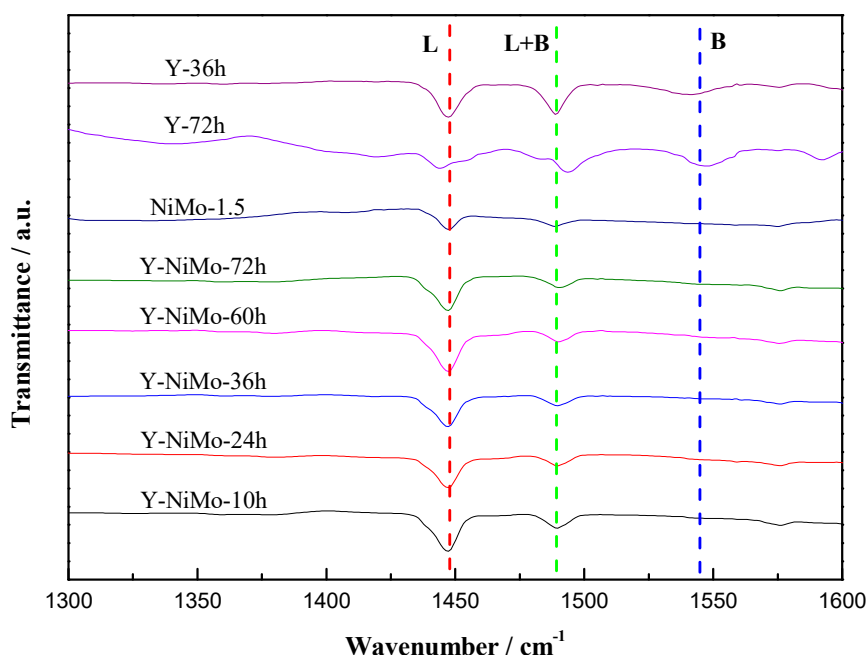


Figure 7. Py-IR spectra of different unsupported NiMo catalysts.

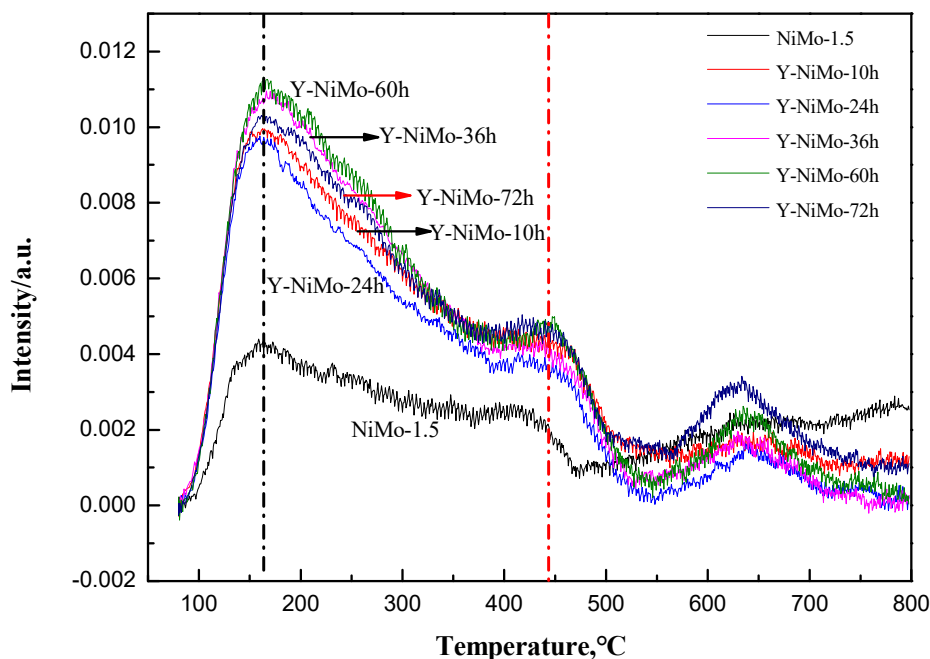


Figure 8. NH_3 -TPD of different unsupported NiMo catalysts.

3.3. Catalytic Performance

Table 4 and Figure 9 show the DBT hydrodesulfurization products, conversion, and DDS/HYD ratios with different unsupported NiMo catalysts at 300 °C. As shown in Figure 9, the catalysts NiMo-1.5, Y-NiMo-10h, and Y-NiMo-24h show high DBT conversion (100%), indicates that the desulfurization activity of the unsupported NiMo catalyst was not affected by the Y-zeolite nanoclusters. In addition, the desulfurization activity of the modified unsupported NiMo catalysts decreases with the prolongation of the crystallization time, indicates that the crystallization time of the Y-zeolite nanoclusters is a key factor affecting the catalytic activity of the unsupported NiMo catalyst, and the desulfurization activity of the unsupported NiMo catalyst could be decreased by the Y-zeolite nanoclusters with too long

a crystallization time. Additionally, compared with the catalysts NiMo-1.5, more biphenyls (BP) were produced for the catalysts Y-NiMo-10h and Y-NiMo-24h (Table 4), and the DDS/HYD of the unsupported NiMo catalysts was higher than NiMo-1.5 (Figure 9), indicated that the Y-zeolite nanoclusters modified catalysts were more likely to desulfurize through the DDS pathway.

Table 4. DBT hydrodesulfurization product distribution of different catalysts at 300 °C, wt%.

Samples	DBT ^a	BP ^b	CHB ^c	BCH ^d	DHP ^e
NiMo-1.5	0	4.1	12.9	23.2	59.8
Y-NiMo-10h	0	18.0	38.0	15.2	28.9
Y-NiMo-24h	0	7.4	26.1	18.7	47.8
Y-NiMo-36h	3.7	17.3	33.0	14.0	31.9
Y-NiMo-60h	4.8	13.6	25.1	16.0	40.5
Y-NiMo-72h	4.2	6.6	28.9	18.8	41.5

^a: Dibenzothiophene. ^b: Biphenyl. ^c: Cyclohexylbenzene. ^d: Bicyclohexane. ^e: Deep Hydrogenation Products.

The TEM results of the sulfided unsupported NiMo catalysts were given in Figure 10. As shown in Figure 10, the concentration of the active components decreased, the reason was that some of the active components were replaced by nanoclusters, which would reduce the content of the active sites. In theory, it is not conducive to the improvement of desulfurization activity of the catalyst. However, the Lewis acid strength of the unsupported NiMo catalyst was improved by the Y-zeolite nanoclusters (Figure 7), and appropriate Lewis acid strength was beneficial to the increase of desulfurization activity of the catalyst [47]. It is the reason why the unsupported NiMo catalysts modified by the Y-zeolite nanoclusters still have high desulfurization activity. However, more nanoclusters structural units will be produced with the prolongation of crystallization time, which will cover more active sites, thus reducing the activity of unsupported NiMo catalysts. The Lewis acid could not make up for the activity loss of the unsupported NiMo catalyst. The desulfurization activity of the modified unsupported NiMo catalysts was finally reduced.

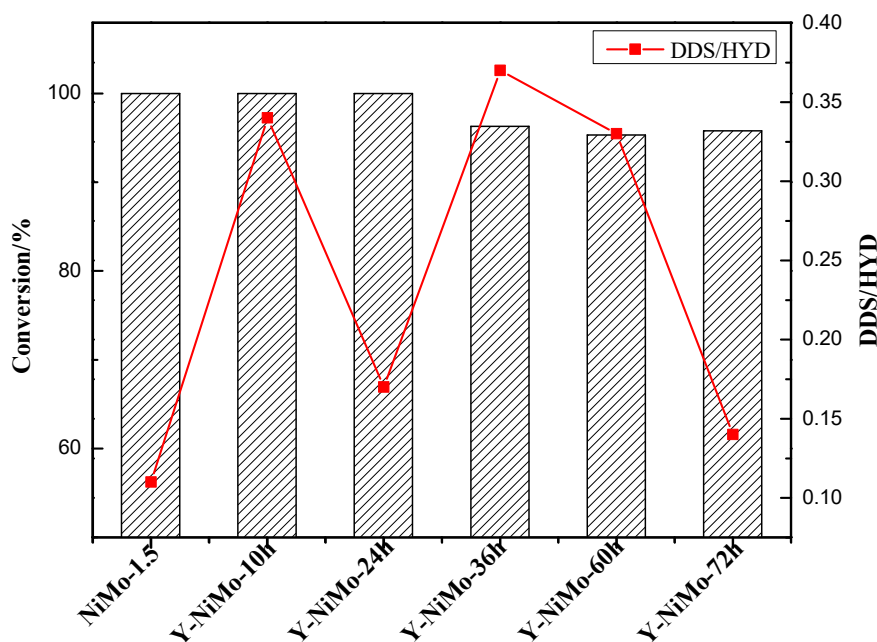


Figure 9. The conversion and DDS/HYD distributions of different unsupported NiMo catalysts.

The desulfurization pathways of the unsupported NiMo catalyst are related to the lamellar length and stacking layers of active component (MoS_2) [48]. The shorter lamellar length and more stacking layers favor direct desulfurization (DDS) and hydrogenation desulfurization (HYD) activity,

respectively [49,50]. The lamellar length and stacking layers distribution of the MoS₂ particles in different unsupported NiMo catalysts was shown in Figures 11 and 12, and the average lamellar length and stacking layers of the MoS₂ particles were also calculated (Table 5).

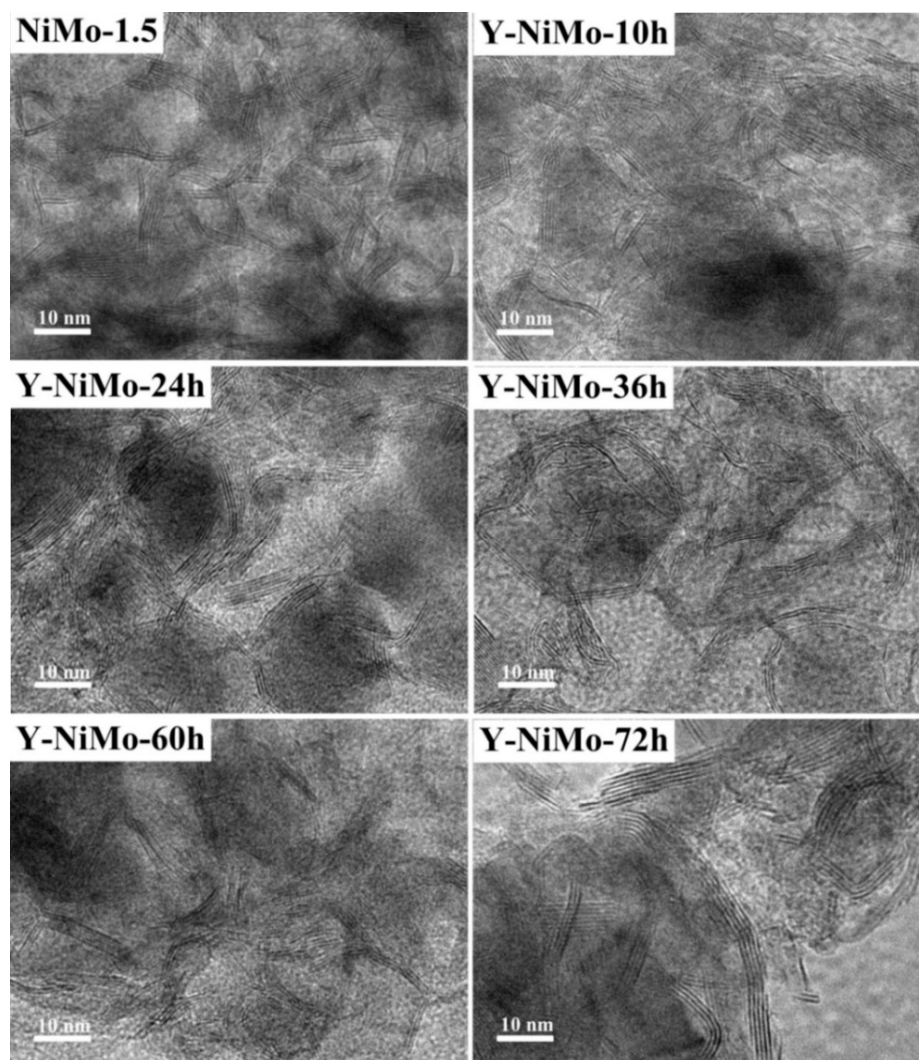


Figure 10. The TEM of sulfided unsupported NiMo catalysts.

The catalysts Y-NiMo-10h and Y-NiMo-24h had shorter MoS₂ lamellar (9.9 and 9.1) and fewer MoS₂ stacking layers (4.5 and 5.2) than the catalyst NiMo-1.5, so it produced the higher proportion of the DDS desulfurization route than the NiMo-1.5 catalyst, which occurred because shorter lamellar length can produce more sulfur vacancies which favor the DDS desulfurization route, and more MoS₂ stacking layers could result in the aggregation of the active components (MoS₂) with higher deep hydrogenation activity. After the introduction of the Y-zeolite nanoclusters, the active components were dispersed and the stacking layers were reduced, which is more favorable to the DDS route. Furthermore, the dispersion frequency of the active phase at edge angle site was also calculated (Table 5), and the catalyst Y-NiMo-24h has higher f_{Mo} (0.13), indicating that the catalyst Y-NiMo-24h has more dispersed edge active sites, which is active for hydrogenolysis (C-S bond breaking). In addition, as the crystallization time of the Y-zeolite nanoclusters was prolonged, the modified catalysts had a longer lamellar length and less MoS₂ stacking layers, which could produce low hydrogenation activity.

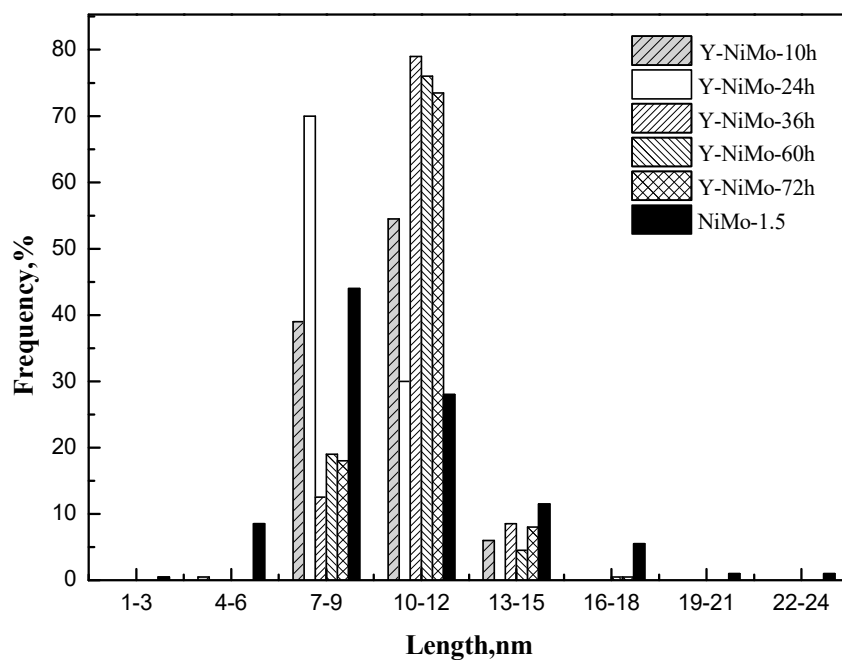


Figure 11. Distributions of slab length of MoS₂ particles on different unsupported NiMo catalysts.

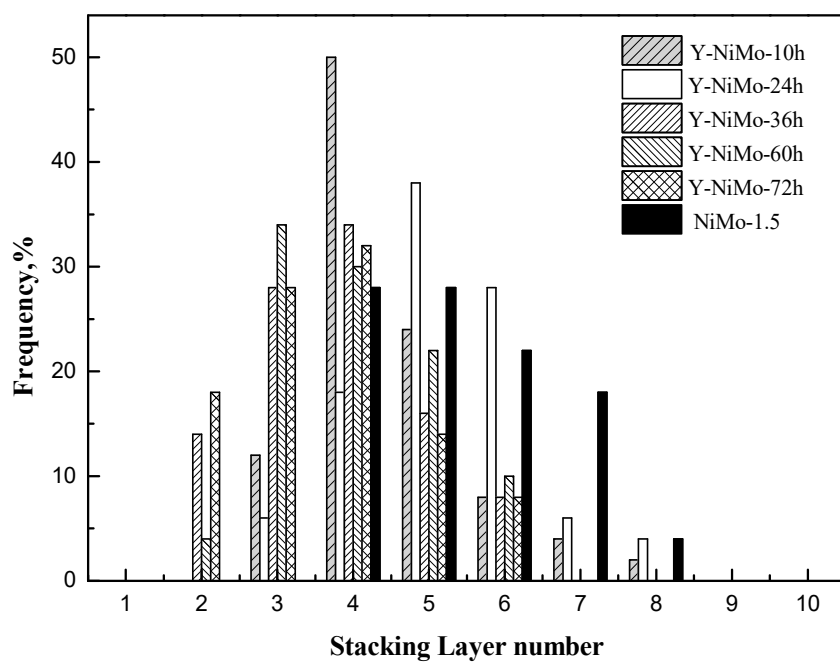


Figure 12. Distributions of stacking layer number of MoS₂ particles on different unsupported NiMo catalysts.

Table 5. Average slab length (L_A) and stacking layer number (N_A) of MoS₂.

Samples	L_A /nm	N_A	f_{Mo}
NiMo-1.5	10.2	5.4	0.11
Y-NiMo-10h	9.9	4.5	0.12
Y-NiMo-24h	9.1	5.2	0.13
Y-NiMo-36h	10.8	3.8	0.11
Y-NiMo-60h	10.5	4.0	0.12
Y-NiMo-72h	10.7	3.7	0.11

On the other hand, the unmodified unsupported NiMo catalyst NiMo-1.5 has higher deep desulfurization activity which can produce more DHP (59.8%), so the higher hydrogen consumption is required. However, high hydrogen consumption is an unfavorable factor for industrial production due to the higher operating costs. The introduction of the Y-zeolite nanoclusters can reduce the deep hydrogenation activity of the unsupported NiMo catalyst which improves the proportion of biphenyls (BP) and decreases the DHP. For the Y-NiMo-10h, the proportion of DHP decreases from 59.8% to 28.9% than NiMo-1.5. It is conducive to reducing hydrogen consumption and saving costs than the unmodified unsupported NiMo catalyst (NiMo-1.5).

3.4. The Action Mechanism of Y-Zeolite Nanoclusters

In order to study the action mechanism of Y-zeolite nanoclusters, the particle size distribution was measured by a laser particle size analyzer (Figure 13). The schematic diagram of Y-zeolite nanoclusters with different crystallization times is shown in Figure 14.

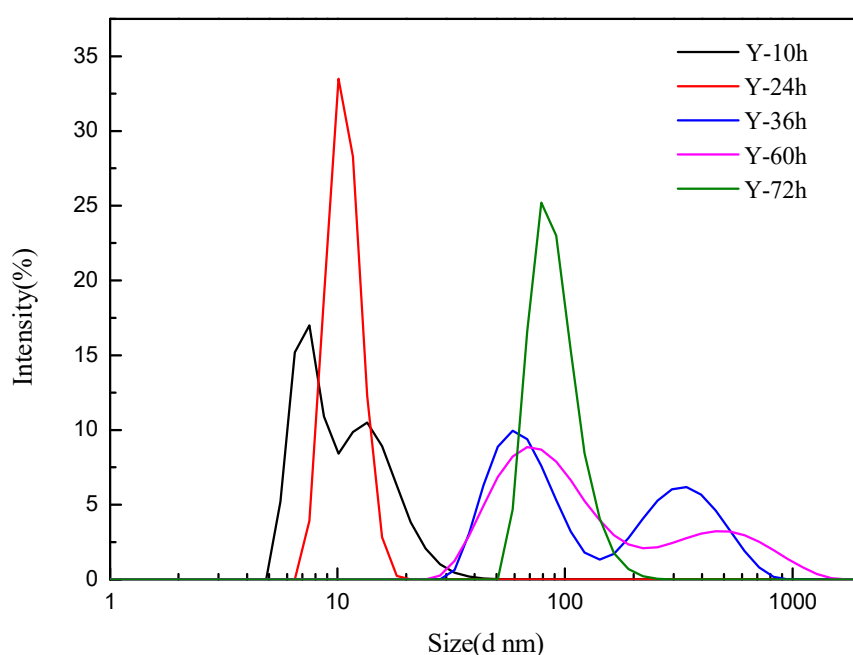


Figure 13. DLS patterns of the Y-zeolite nanoclusters of different crystallizing times.

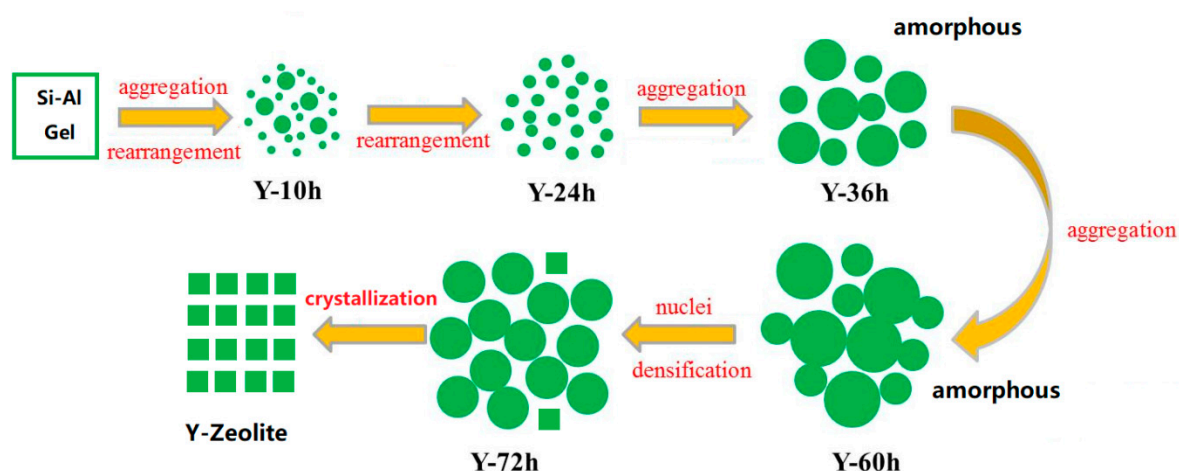


Figure 14. The schematic diagram of Y-zeolite nanoclusters with different crystallization times.

As shown in Figures 13 and 14, when the crystallization time is 10 h, most of the samples are in gel state, and the particle size distribution of nanoclusters is uneven. When the crystallization time is 24 h, the DLS shows a narrower range of particle size distribution, indicating that the nanocluster particles become uniform by rearrangement, and then the uniform nanocluster particles gather to form clusters with uneven particle size. Finally, these clusters will form zeolite nanocrystals by rearrangement and crystallization. The Y-24 h has a smaller and more uniform particle size distribution, so it is easier for nanoclusters to enter the interlamellar space of the unsupported NiMo catalysts, and fewer nanoclusters are exposed to the outer surface of unsupported NiMo catalysts which results in less Lewis acid and total acid content than other catalysts (Tables 2 and 3). On the other hand, for Y-NiMo-24h, less active components in the unsupported NiMo catalysts are covered due to less nanocluster distribution on the outer surface, which is beneficial to higher hydrogenation activity, so the desulfurization was more inclined to the HYD pathway (Figure 9).

4. Conclusions

The Y-zeolite nanoclusters were synthesized successfully to modify the unsupported NiMo catalysts. The specific surface area, pore volume, and average pore size of the unsupported NiMo catalysts modified by the Y-zeolite nanoclusters were increased obviously, and the dispersion of the unsupported NiMo catalysts was improved. The Lewis acid and total acid of the unsupported NiMo catalysts were improved by the Y-zeolite nanoclusters. The DBT HDS results showed that the crystallization time of the Y-zeolite nanoclusters was an important factor affecting the desulfurization activity of the catalysts, the desulfurization activity of the modified catalysts decreased with the increased crystallization time of the Y-zeolite nanoclusters, and when the crystallization time was 10–24 h, the modified catalysts showed higher DBT desulfurization rate.

Author Contributions: Conceptualization, C.Y. and C.D.; methodology, C.Y. and C.D.; software, C.D.; validation, C.Y., C.D., D.L. and C.L.; formal analysis, C.Y. and C.D.; investigation, C.D., T.W. and Z.W.; resources, C.Y. and C.L.; data curation, C.D. and C.Y.; writing—original draft preparation, C.D.; writing—review and editing, C.Y., C.D., D.L. and C.L.; visualization, C.Y. and C.D.; supervision, C.Y., D.L. and C.L.; project administration, C.Y.; funding acquisition, C.Y.

Funding: This work was financially supported by the National Natural Science Fund of China (grant no. 21676301), Shandong Province Natural Science Foundation (grant no. ZR2016BM19), and the National Key R and D program of China (2017YFB0602500).

Acknowledgments: Financial support from China SCHOLARSHIP Fund and PetroChina Corporation Limited was greatly appreciated.

Conflicts of Interest: The authors declare no conflict of interest.

References

1. Olivas, A.; Galván, D.H.; Alonso, G.; Fuentes, S. Trimetallic NiMoW unsupported catalysts for HDS. *Appl. Catal. A Gen.* **2009**, *352*, 10–16. [[CrossRef](#)]
2. Bocarando, J.; Huirache-Acuña, R.; Bensch, W.; Huang, Z.D.; Petranovskii, V.; Fuentes, S.; Alonso-Núñez, G. Unsupported Ni-Mo-W sulphide HDS catalysts with the varying nickel concentration. *Appl. Catal. A Gen.* **2009**, *363*, 45–51. [[CrossRef](#)]
3. Yoosuk, B.; Kim, J.H.; Song, C.; Ngamcharussrivichai, C.; Prasassarakich, P. Highly active MoS₂, CoMoS₂ and NiMoS₂ unsupported catalysts prepared by hydrothermal synthesis for hydrodesulfurization of 4,6-dimethyldibenzothiophene. *Catal. Today* **2008**, *130*, 14–23. [[CrossRef](#)]
4. Zhang, L.; Afanasiev, P.; Li, D.; Long, X.; Vrinat, M. Solution synthesis of unsupported Ni–W–S hydrotreating catalysts. *Catal. Commun.* **2007**, *8*, 2232–2237. [[CrossRef](#)]
5. Korányi, T.I.; Manninger, I.; Paál, Z.; Marks, O.; Günter, J.R. Activation of unsupported CoMo catalysts in thiophene hydrodesulfurization. *J. Catal.* **1989**, *116*, 422–439. [[CrossRef](#)]
6. González-Cortés, S.L. Comparing the hydrodesulfurization reaction of thiophene on γ -Al₂O₃ supported CoMo, NiMo and NiW sulfide catalysts. *React. Kinet. Catal. Lett.* **2009**, *97*, 131–139. [[CrossRef](#)]

7. Yongchul, P.; Eunsuok, O.A.; Rhee, H.K. Characterization and catalytic activity of WNiMo/Al₂O₃ catalyst for hydrodenitrogenation of pyridine. *Ind. Eng. Chem. Res.* **1997**, *36*, 5083–5089.
8. Egorova, M.; Prins, R. Hydrodesulfurization of dibenzothiophene and 4,6-dimethyldibenzothiophene over sulfided NiMo/γ-Al₂O₃, CoMo/γ-Al₂O₃, and Mo/γ-Al₂O₃ catalysts. *J. Catal.* **2004**, *225*, 417–427. [[CrossRef](#)]
9. Liu, H.; Liu, Q.; Zhang, J.; Yin, C.; Zhao, Y.; Yin, S.; Liu, C.; Sun, W. PVP-assisted synthesis of unsupported NiMo catalysts with enhanced hydrodesulfurization activity. *Fuel Process. Technol.* **2017**, *160*, 93–101. [[CrossRef](#)]
10. Liu, H.; Yin, C.; Li, X.; Chai, Y.; Li, Y.; Liu, C. Effect of NiMo phases on the hydrodesulfurization activities of dibenzothiophene. *Catal. Today* **2017**, *282*, 222–229. [[CrossRef](#)]
11. Liu, H.; Liu, C.; Yin, C.; Liu, B.; Li, X.; Li, Y.; Chai, Y.; Liu, Y. Low temperature catalytic hydrogenation naphthalene to decalin over highly-loaded NiMo, NiW and NiMoW catalysts. *Catal. Today* **2016**, *276*, 46–54. [[CrossRef](#)]
12. Amaya, S.L.; Alonso-Núñez, G.; Cruz-Reyes, J.; Fuentes, S.; Echavarría, A. Influence of the sulfidation temperature in a NiMoW catalyst derived from layered structure (NH₄)Ni₂OH(H₂O)(MoO₄)₂. *Fuel* **2015**, *139*, 575–583. [[CrossRef](#)]
13. Espino, J.; Alvarez, L.; Ornelas, C.; Rico, J.L.; Fuentes, S.; Berhault, G.; Alonso, G. Comparative study of WS₂ and Co(Ni)/WS₂ HDS catalysts prepared by ex situ / in situ activation of ammonium thiotungstate. *Catal. Lett.* **2003**, *90*, 71–80. [[CrossRef](#)]
14. Gochi, Y.; Ornelas, C.; Paraguay, F.; Fuentes, S.; Alvarez, L.; Rico, J.L.; Alonso-Núñez, G. Effect of sulfidation on Mo-W-Ni trimetallic catalysts in the HDS of DBT. *Catal. Today* **2005**, *107–108*, 531–536. [[CrossRef](#)]
15. Wang, T.F.; Ye, Z.; Hui, G.E.; Tang, M.X.; Zhou, L.G.; Lv, Z.; Li, X. Hydrodesulfurization of thiophene over Mo/AC catalyst presulfided by ammonium thiosulfate. *J. Fuel Chem. Technol.* **2015**, *43*, 202–207. [[CrossRef](#)]
16. Yin, C.; Wang, Y.; Xue, S.; Liu, H.; He, L.; Liu, C. Influence of sulfidation conditions on morphology and hydrotreating performance of unsupported Ni–Mo–W catalysts. *Fuel* **2016**, *175*, 13–19. [[CrossRef](#)]
17. Yin, C.; Dong, C.; Kong, Y.; Li, K.; Zhang, H.; Liu, D.; Liu, C. Effects of aging treatment on the hydrotreating performance of the unsupported catalyst. *Ind. Eng. Chem. Res.* **2019**, *58*, 2683–2688. [[CrossRef](#)]
18. Dong, C.; Yin, C.; Wu, T.; Wu, Z.; Liu, D.; Liu, C. Effect of β-zeolite nanoclusters on the acidity and hydrodesulfurization activity of an unsupported NiMo catalyst. *Catal. Commun.* **2019**, *119*, 164–169. [[CrossRef](#)]
19. Abbot, J. Role of Brønsted and Lewis acid sites during cracking reactions of alkanes. *Appl. Catal.* **1989**, *47*, 33–44. [[CrossRef](#)]
20. Schallmoser, S.; Ikuno, T.; Wagenhofer, M.F.; Kolvenbach, R.; Haller, G.L.; Sanchez-Sanchez, M.; Lercher, J.A. Impact of the local environment of Brønsted acid sites in ZSM-5 on the catalytic activity in n-pentane cracking. *J. Catal.* **2014**, *316*, 93–102. [[CrossRef](#)]
21. D’Ippolito, S.A.; Especel, C.; Vivier, L.; Epron, F.; Pieck, C.L. Influence of the Brønsted acidity, SiO₂/Al₂O₃ ratio and rh–pd content on the ring opening: Part I. Selective ring opening of decalin. *Appl. Catal. A Gen.* **2014**, *469*, 532–540. [[CrossRef](#)]
22. Kubička, D.; Kumar, N.; Mäki-Arvela, P.; Tiitta, M.; Niemi, V.; Salmi, T.; Murzin, D.Y. Ring opening of decalin over zeolites. I. Activity and selectivity of proton-form zeolites. *J. Catal.* **2004**, *222*, 65–79. [[CrossRef](#)]
23. Ferraz, S.G.A.; Zotin, F.M.Z.; Araujo, L.R.R.; Zotin, J.L. Influence of support acidity of NiMoS catalysts in the activity for hydrogenation and hydrocracking of tetralin. *Appl. Catal. A Gen.* **2010**, *384*, 51–57. [[CrossRef](#)]
24. Kirschhock, C.E.A.; Ravishankar, R.; Verspeurt, F.; Grobet, P.J.; And, P.A.J.; Martens, J.A. Identification of precursor species in the formation of MFI zeolite in the TPAOH-TEOS-H₂O system. *J. Phys. Chem. B* **1999**, *103*, 4965–4971. [[CrossRef](#)]
25. Kirschhock, C.E.A.; Ravishankar, R.; Verspeurt, F.; Grobet, P.J.; And, P.A.J.; Martens, J.A. Reply to the comment on “identification of precursor species in the formation of MFI zeolite in the TPAOH-TEOS-H₂O system”. *J. Phys. Chem. B* **2002**, *106*, 3329–3332. [[CrossRef](#)]
26. Prokešová, P.; Mintova, S.; Čejka, J.; Bein, T. Preparation of nanosized micro/mesoporous composites. *Mater. Sci. Eng. C* **2003**, *23*, 1001–1005. [[CrossRef](#)]
27. Frunz, L.; Prins, R.; Pirngruber, G.D. ZSM-5 precursors assembled to a mesoporous structure and its subsequent transformation into a zeolitic phase—from low to high catalytic activity. *Microporous Mesoporous Mater.* **2006**, *88*, 152–162. [[CrossRef](#)]

28. Tsapatsis, M.; Lovallo, M.; Okubo, T.; Davis, M.E.; Sadakata, M. Characterization of zeolite L nanoclusters. *Chem. Mater.* **1995**, *7*, 1734–1741. [[CrossRef](#)]
29. Li, Y.; Chi, K.; Zhang, H.; Du, P.; Hu, D.; Xiao, C.; Li, H.; Zhao, Z.; Duan, A.; Xu, C. The influence of hydrothermal crystallization temperature on a novel FDU-12 mesoporous composite assembled by ZSM-5 nanoclusters and its hydrodesulfurization performance for DBT and FCC diesel. *Fuel Process. Technol.* **2018**, *180*, 56–66. [[CrossRef](#)]
30. Liu, H.; Yin, C.; Liu, B.; Li, X.; Li, Y.; Chai, Y.; Liu, C. Effect of calcination temperature of unsupported NiMo catalysts on the hydrodesulfurization of dibenzothiophene. *Energy Fuels* **2014**, *28*, 2429–2436. [[CrossRef](#)]
31. Larlus, O.; Mintova, S.; Bein, T. Environmental syntheses of nanosized zeolites with high yield and monomodal particle size distribution. *Microporous Mesoporous Mater.* **2006**, *96*, 405–412. [[CrossRef](#)]
32. Zuo, D.; Vrinat, M.; Nie, H.; Maugé, F.; Shi, Y.; Lacroix, M.; Li, D. The formation of the active phases in sulfided NiW/Al₂O₃ catalysts and their evolution during post-reduction treatment. *Catal. Today* **2004**, *93*, 751–760. [[CrossRef](#)]
33. Yin, H.-L.; Liu, X.-L.; Zhou, T.-N.; Lin, A.-G. Effect of preparation method of nanosized zeolite HY-Al₂O₃ composite as NiMo catalyst support on diesel HDS. *J. Fuel Chem. Technol.* **2018**, *46*, 950–956. [[CrossRef](#)]
34. Hensen, E.J.M.; Kooyman, P.J.; van der Meer, Y.; van der Kraan, A.M.; de Beer, V.H.J.; van Veen, J.A.R.; van Santen, R.A. The relation between morphology and hydrotreating activity for supported MoS₂ particles. *J. Catal.* **2001**, *199*, 224–235. [[CrossRef](#)]
35. Méndez, F.J.; Franco-López, O.E.; Bokhimi, X.; Solís-Casados, D.A.; Escobar-Alarcón, L.; Klimova, T.E. Dibenzothiophene hydrodesulfurization with NiMo and CoMo catalysts supported on niobium-modified MCM-41. *Appl. Catal. B: Environ.* **2017**, *219*, 479–491. [[CrossRef](#)]
36. Ding, L.; Ying, Z.; Zhang, Z.; Chen, J. Hydrotreating of light cycled oil using WNi/Al₂O₃ catalysts containing zeolite beta and/or chemically treated zeolite Y. *J. Catal.* **2006**, *241*, 435–445. [[CrossRef](#)]
37. Prokešová, P.; Mintova, S.; Čejka, J.; Bein, T. Preparation of nanosized micro/mesoporous composites via simultaneous synthesis of beta/MCM-48 phases. *Microporous Mesoporous Mater.* **2003**, *64*, 165–174. [[CrossRef](#)]
38. Zhao, J.; Yin, Y.; Li, Y.; Chen, W.; Liu, B. Synthesis and characterization of mesoporous zeolite Y by using block copolymers as templates. *Chem. Eng. J.* **2016**, *284*, 405–411. [[CrossRef](#)]
39. Huang, Y.; Wang, K.; Dong, D.; Li, D.; Hill, M.R.; Hill, A.J.; Wang, H. Synthesis of hierarchical porous zeolite NaY particles with controllable particle sizes. *Microporous Mesoporous Mater.* **2010**, *127*, 167–175. [[CrossRef](#)]
40. Ikuno, T.; Chaikittisilp, W.; Liu, Z.; Iida, T.; Yanaba, Y.; Yoshikawa, T.; Kohara, S.; Wakihara, T.; Okubo, T. Structure-directing behaviors of tetraethylammonium cations toward zeolite beta revealed by the evolution of aluminosilicate species formed during the crystallization process. *JACS J. Am. Chem. Soc.* **2015**, *137*, 14533–14544. [[CrossRef](#)]
41. Levin, D.; Ying, J.Y. Oxidative dehydrogenation of propane by non-stoichiometric nickel molybdates. *Stud. Surf. Sci. Catal.* **1997**, *110*, 367–373.
42. Levin, D.; Soled, S.L.; Ying, J.Y. Crystal structure of an ammonium nickel molybdate prepared by chemical precipitation. *Inorg. Chem.* **1996**, *35*, 4191–4197. [[CrossRef](#)] [[PubMed](#)]
43. Lin, S.L.; Hwang, C.S.; Lee, J.F. Characterization of CeO–Al₂O₃–SiO₂ glasses by infrared and X-Ray absorption near edge structure spectroscopies. *J. Mater. Res.* **1996**, *11*, 2641–2650. [[CrossRef](#)]
44. Pelmenschikov, A.G.; Wolput, J.H.M.C.V.; Jaenchen, J.; Santen, R.A.V. (a,b,c) triplet of infrared OH bands of zeolitic H-complexes. *J. Phys. Chem.* **1995**, *99*, 3612–3617. [[CrossRef](#)]
45. Flanigen, E.M. Infrared structural studies of zeolite frameworks. *Adv. Chem.* **1971**, *101*, 201–229.
46. Wang, Y.; Ma, J.; Liang, D.; Zhou, M.; Li, F.; Li, R. Lewis and Brønsted acids in super-acid catalyst SO₄²⁻/ZrO₂-SiO₂. *J. Mater. Sci.* **2009**, *44*, 6736–6740. [[CrossRef](#)]
47. Weissman, J.G. Niobia-alumina supported hydroprocessing catalysts: Relationship between activity and support surface acidity. *Catal. Today* **1996**, *28*, 159–166. [[CrossRef](#)]
48. Zhao, R.Y.; Zeng, L.Y.; Liang, J.; Liu, C.G. Interaction between Ni promoter and Al₂O₃ support and its effect on the performance of NiMo/γ-Al₂O₃ catalyst in hydrodesulfurization. *J. Fuel Chem. Technol.* **2016**, *44*, 564–569. [[CrossRef](#)]

49. Liu, X.; Li, X.; Yan, Z. Facile route to prepare bimodal mesoporous γ -Al₂O₃ as support for highly active CoMo-based hydrodesulfurization catalyst. *Appl. Catal. B Environ.* **2012**, *121–122*, 50–56. [[CrossRef](#)]
50. Vradman, L.; Landau, M.V. Structure–function relations in supported Ni–W sulfide hydrogenation catalysts. *Catal. Lett.* **2001**, *77*, 47–54. [[CrossRef](#)]



© 2019 by the authors. Licensee MDPI, Basel, Switzerland. This article is an open access article distributed under the terms and conditions of the Creative Commons Attribution (CC BY) license (<http://creativecommons.org/licenses/by/4.0/>).